Applied Catalysis B: Environmental 278 (2020) 119261

Contents lists available at ScienceDirect

Applied Catalysis B: Environmental

journal homepage: www.elsevier.com/locate/apcatb

Dopamine sacrificial coating strategy driving formation of highly active surface-exposed Ru sites on Ru/TiO_2 catalysts in Fischer–Tropsch synthesis

Shuaishuai Lyu[a,b,c], Qingpeng Cheng[a,b], Yunhao Liu[a,b], Ye Tian[a,b], Tong Ding[a,b], Zheng Jiang[d], Jing Zhang[e], Fei Gao[f], Lin Dong[f], Jun Bao[g], Qingxiang Ma[h], Quan-Hong Yang[a,c], Xingang Li[a,b,*]

[a] Collaborative Innovation Center for Chemical Science & Engineering (Tianjin), State Key Laboratory of Chemical Engineering, School of Chemical Engineering and Technology, Tianjin University, Tianjin, 300072, PR China
[b] Tianjin Key Laboratory of Applied Catalysis Science & Engineering, Tianjin, 300072, PR China
[c] Nanoyang Group, 300072, PR China
[d] Shanghai Synchrotron Radiation Facility, Shanghai Institute of Applied Physics, Chinese Academy of Sciences, Shanghai, 201800, PR China
[e] Beijing Synchrotron Radiation Facility, Institute of High Energy Physics, Chinese Academy of Sciences, Beijing, 100049, PR China
[f] Jiangsu Key Laboratory of Vehicle Emissions Control, Center of Modern Analysis, Nanjing University, Nanjing, 21009, PR China
[g] National Synchrotron Radiation Laboratory, University of Science and Technology of China, Hefei, 230029, PR China
[h] State Key Laboratory of High-efficiency Coal Utilization and Green Chemical Engineering, Ningxia University, Yinchuan, 750021, PR China

ARTICLE INFO

Keywords:
Fischer–Tropsch synthesis
Ru/TiO_2
Active sites
Dopamine sacrificial coating
metal–support interactions

ABSTRACT

Generally, strong metal–support interactions of reducible metal oxides supports will cause encapsulation of suboxides on metal catalysts. It inevitably brings the formation of metal–support interfacial sites, and decreases surface-exposed metal sites. Herein, we synthesize Ru/TiO_2 catalysts through a dopamine sacrificial coating strategy, which significantly increases the number of surface-exposed Ru sites with the high dispersion. The as-synthesized Ru/TiO_2-500-H catalyst exhibits the high Fischer–Tropsch synthesis performance and catalytic stability. We discover that the TOF of surface-exposed Ru sites is 5.3-fold that of interfacial ones in our catalyst system. Moreover, surface-exposed Ru sites could thermal-stably adsorb CO, stimulate the chain growth and promote the C_{5+} selectivity by strengthening the bond between CH_x intermediates and metal sites, as evidenced by in situ characterizations operated under real operating conditions. Our findings provide comprehensive understandings of rationally designing highly efficient metal catalysts, which can be potentially applied in other related catalysis systems.

1. Introduction

Fischer–Tropsch synthesis (FTS) is one of the efficient approaches for converting syngas (CO and H_2) derived from non-petroleum carbon sources including natural gas, coal and biomass into clean hydrocarbon fuels and value-added chemicals over metal catalysts [1–3]. It is a complex heterogeneous catalytic process and proceeds through several key elementary steps in the whole reaction, mainly including (1) adsorption and dissociation of CO and H_2, (2) formation of surface CH_x intermediates, (3) C–C bond coupling for chain growth, and (4) dehydrogenation and hydrogenation [1].

Supported Ru catalysts have been regarded as promising candidates in FTS with advantages of the superior activity, selectivity towards long-chain hydrocarbons and stability under harsh reaction conditions [4–7]. TiO_2 is one of the conventional supports, which can generate classical strong metal–support interactions (SMSI) emanating from the encapsulation of metal nanoparticles (NPs) by metal oxide supports [8–10]. Some papers have reported that SMSI can promote catalytic reactions due to the generation of new active sites at metal–support interfaces created by coverage of oxide layers on metal particles. Uematsu et al. reported the enhanced CO_2 hydrogenation performance over Ru/TiO_2 catalysts resulting from the generation of active sites at metal–support perimeters [11]. Bell et al. also found that the FTS performance over the Ru/TiO_2 catalyst was dominated by the migrated TiO_x layer, which could provide more active interfacial sites for CO dissociation [12]. Notably, this encapsulation behavior on metal catalysts induced by SMSI could even occur at low reduction temperatures like 300 °C [11,13–15]. Thus, it is difficult to be avoided in FTS, which generally requires the pre-reduction of metal catalysts above 300 °C prior to the reaction. However, the dense overlayer of suboxides on the

* Corresponding author at: Collaborative Innovation Center for Chemical Science & Engineering (Tianjin), State Key Laboratory of Chemical Engineering, School of Chemical Engineering and Technology, Tianjin University, Tianjin, 300072, PR China.
E-mail address: xingang_li@tju.edu.cn (X. Li).

https://doi.org/10.1016/j.apcatb.2020.119261
Received 19 March 2020; Received in revised form 15 June 2020; Accepted 19 June 2020
Available online 21 June 2020

metal particles might block the access of reactants to available active sites, limiting the catalytic reaction from further proceeding [16,17].

Several strategies are proposed to deal with the issue of the active site blockage induced by SMSI to improve the catalytic activity. de Jong et al. exploited the cyclic reduction–oxidation–reduction (ROR) treatment on the Co/TiO_2 FTS catalysts. The ROR modulation effectively doubled the number of available Co sites through decreasing the size of Co NPs to promote the apparent catalytic performance without changing their intrinsic activity (turnover frequency, TOF) [17]. Christopher et al. [18] and Wang et al. [19] constructed reactant-permeable TiO_x overlayers on metal catalysts to increase the number of accessible active sites for reactants. Li et al. enwrapped a functionalized hydrothermal carbon (HTC) layer on the TiO_2 support before the deposition of cobalt to avoid the encapsulation of TiO_2 on metal sites, which led to the increase in exposed active sites in metal catalysts. By controlling the thickness of the HTC layer and annealing temperature, the FTS activity was optimized [20]. Dai et al. have reported that the dopamine sacrificial coating strategy for Au/TiO_2 could improve the MSI and electronic interactions and finally construct the sintering-resistant Au NPs [21]. This strategy changes both the geometric contact and electronic interaction between metal and support during the catalyst preparation, and offers the possibility to tune the number of surface-exposed metal sites and interfacial metal sites on the TiO_2 support. Up to now, few studies have clarified the difference between surface-exposed and interfacial metal sites in FTS, which might significantly determine the catalytic performance [22].

In this study, aqueous-phase route [23,24] and dopamine sacrificial coating strategy [21] are combined for the preparation of the Ru/TiO_2 catalysts. By changing the calcination temperatures during the dopamine modification process, we successfully prepare the Ru/TiO_2 catalysts with the average diameter of Ru NPs at around 3 nm. Our strategy could form more surface-exposed metallic Ru sites and suppress the formation of interfacial Ru sites originating from the support encapsulation. The former exhibited excellent thermal stability for CO adsorption than the latter. Moreover, we interestingly discover that the TOF of surface-exposed Ru sites is 5.3-fold that of interfacial Ru sites. Due to possessing the largest number of surface-exposed Ru sites, the Ru/TiO_2-500-H catalyst exhibits the highest FTS activity. In addition, the thermal-stable linear-adsorbed CO species on surface-exposed Ru sites facilitate the chain-growth of hydrocarbons to produce heavy FTS products due to the strong bond between CH_x intermediates and metallic Ru sites. Our results could offer novel perspectives on rationally designing highly active metal FTS catalysts.

2. Experimental methods

2.1. Catalyst preparation

Ru/TiO_2 was prepared by the chemical-reduction method reported previously [21,23,24]. In a typical synthesis, $RuCl_3{\cdot}xH_2O$ and ε-Amino-*n*-caproic Acid (denoted as EACA) (the mass ratio of $RuCl_3{\cdot}xH_2O$: EACA equaling to 1:2) were dispersed in deionized water after ultrasonic treatment. 0.5 g commercial TiO_2 (Degussa P25) was then added to the mixture under vigorous magnetic stirring. Thereafter, excess $NaBH_4$ solution was added to the mixture solution dropwise to make Ru^{3+} get fully reduced to Ru°. Then the whole mixture was transferred into the oil boil and stirred at 90 °C for 3 h. After the solution was cooled down to room temperature, the catalyst was centrifuged and washed by deionized water and absolute ethanol for several times to assure that all Cl^- was completely removed. $AgNO_3$ aqueous solution was used to test the residual Cl- in the catalyst and no Cl^- was detected. Finally, the obtained sample was dried overnight and named as Ru/TiO_2. The Ru loading was determined to be 4.7 wt % by inductively coupled plasma-optical emission spectrometry (ICP-OES, VIISTA-MPX, Varian). This value was less than the theoretical content 5.7 %, which might be ascribed to the washing process during the synthesis process.

For the synthesis of Ru/TiO_2@DA, 100 mg dopamine (DA) was added to 100 mL tris-buffer solution under vigorous stirring at room temperature for 1 h. Then the as-prepared Ru/TiO_2 was dispersed in the above mixture and stirred for 24 h. The suspension was separated by centrifugation and then washed by deionized water and absolute ethanol for several times. Later, the sample was dried in vacuum at 70 °C overnight. The as-prepared Ru/TiO_2@DA was subjected to the annealing treatment at 700 °C in N_2 flow for 2 h, and the resulting sample was denoted as Ru/TiO_2@carbon.

Ru/TiO_2-*T* catalysts were obtained by directly heating Ru/TiO_2@carbon in air at different temperatures, in which *T* presents the calcination temperature of 500/600/700 °C for 2 h, while Ru/TiO_2-500# was obtained by the direct calcination of Ru/TiO_2 in air at 500 °C. No Ru loss was observed during the calcination procedure, as evidenced by the ICP results.

2.2. Catalyst characterization

Transmission electron microscopy (TEM) and high-resolution transmission electron microscopy (HRTEM) were performed by a JEOL JEM-2100 F transmission electron microscope operating at 200 kV. The catalysts were reduced in H_2 flow at 300 °C for 3 h and then added in the ethanol. After ultrasonic treatment, the suspension was deposited on the copper grids for the TEM tests. The average particle size was calculated upon the measurement of 200 particles collecting from different positions of copper grids.

The measurements of specific surface area (S_{BET}) and pore volume (*PV*) were carried out on a Quantachrome QuadraSorb SI instrument at −196 °C by nitrogen adsorption-desorption. Before the analysis, the catalysts were degassed at 200 °C for 3 h to remove adsorbed H_2O and other impure surface species. The S_{BET} was determined from the linear part of the BET curve, and *PV* was determined by the Barrett-Joyner-Halenda (BJH) method from the desorption branch of the isotherm.

The X-ray diffraction (XRD) patterns of the catalysts were recorded on a Bruker D8 focus diffraction instrument operating at 200 mA and 40 kV. The radiation source was Cu K_α (λ = 0.15418 nm) and all patterns were collected at a scan speed of 0.133° s^{-1} in the 2θ from 20° to 90°, except for the slow scanning of 2θ from 26° to 29°, the scan speed is 0.017° s^{-1}.

Visible Raman spectra were obtained on a Raman spectrometer (Renishaw, inVia reflex) using a laser wavelength of 532 nm.

The spectra of in situ X-ray photoelectron spectroscopy (XPS) were recorded on a PHI 5000 versa Probe with an aluminum anode (Al $K\alpha$ = 148.6 eV) operating at 25 W. The as-prepared catalysts were put in the introduction chamber (IC) and then transferred to the reaction chamber (RC) by a transfer rod. All catalysts were reduced in H_2 at 300 °C for 3 h after degassing the RC. Once the temperature cooled down to room temperature, the catalysts were transferred back to IC and degassed again to remove the adsorbed H_2. Subsequently, the catalysts were transferred to the main chamber for the latter XPS detection with an accuracy of ± 0.1 eV. The C 1*s* peak (284.6 eV) was used as the standard to calibrate the binding energies.

The H_2 temperature-programmed reduction (H_2-TPR) operations were carried out on a TPDRO apparatus (TP-5080, Tianjin Xianquan Co. Ltd). Typically, 30 mg catalyst was loaded into the quartz tube reactor and then pretreated in He flow for 1 h to remove adsorbed impurities, followed by heating the catalysts from room temperature to 900 °C at the heating rate of 10 °C min^{-1} in 8.0 vol % H_2/N_2 flow (30 mL min^{-1}).

The H_2 temperature-programmed desorption (H_2-TPD) experiments were carried out to determine the dispersion of catalysts on the above TPDRO apparatus. In a typical experiment, 200 mg catalyst was loaded in the quartz tube reactor and reduced at 300 °C at the rate of 5 °C

min^{-1} for 3 h in H_2 flow, which was then switched to N_2 flow for 0.5 h to remove the adsorbed impurities on the catalyst surface. Then, the whole system was switched to H_2 flow again at 100 °C for 1 h to fully adsorb H_2, followed by the purging process in N_2 flow at 100 °C for 0.5 h. Finally, the temperature was linearly increased up to 900 °C at the rate of 10 °C min^{-1} in N_2 flow for the TPD analysis. The adsorption stoichiometry factor of H_2 is assumed to be 2, *i.e.*, one H atom on per ruthenium atom. The total H_2-uptake from the isotherm was used to determine the amount of metallic Ru atoms exposed on the surface and calculate the dispersion. This value was also employed to calculate the accessible Ru surface area based on the Ru atomic surface area (0.0817 nm^2 $atom^{-1}$) [25].

The thermal gravimetric (TG) analysis was carried out on a Perkin-Elmer Diamond TG/DTA instrument. About 6 mg catalyst was heated from room temperature to 900 °C in air or N_2 flow (100 mL min^{-1}) at the heating rate of 10 °C min^{-1}.

The photoluminescence (PL) measurement was performed on the Horiba Jobin Yvon Fluorolog3 photoluminescence spectrometer at room temperature using the excitation wavelength of 325 nm.

In situ DRIFTS spectra were collected by using Fourier transform infrared spectroscope (Thermo Fisher, Nicolet IS50) equipped with a commercial in situ reaction cell. The spectra were recorded with a Magna 6700 spectrometer (Thermo) equipped with an MCT narrow-band detector. The scan number was 256 and the spectral resolution was set as 4 cm^{-1}. All catalysts were pre-reduced in H_2 flow for 3 h (ambient pressure). The cell was then flushed in He flow at 300 °C for 0.5 h to remove the resident H_2 on the catalysts and in the cell. After the system was cool down to room temperature, the background was recorded to analyze the followed spectra collected under in situ conditions. The syngas (H_2/CO = 2) or CO (> 99.9 %) was used as the probe gas at the desired temperatures. The back-pressure valve was used to make sure that the pressure of the adsorption gas was kept at 2 MPa. There are mainly three procedures for in situ DRIFTS experiments. In procedure A, the reduced catalysts were first exposed to CO (> 99.9 %, 2 MPa) for 0.5 h at 220 °C and then the He flow was used as flush gas at 220 °C for 0.5 h to remove gaseous CO in the reaction chamber. The spectra were collected during the steady-state in which the chemically adsorbed CO species on catalysts keep unchanged furthermore. In procedure B, the CO adsorption (2 MPa) was performed at 50 °C for 0.5 h and most of the gaseous CO was purged with He at the same temperature for 0.5 h. Thereafter, the temperature was increased to 220 °C at a rate of 5 °C min^{-1} in flowing He and the spectra were recorded for every 10 °C. The details of the procedure C were similar to the procedure A except that the probe gas was changed to syngas (H_2/CO = 2, 2 MPa).

X-ray absorption fine structures (XAFS) at the Ru *K* edge (22117 eV) were collected by using fluorescence mode at the BL14W1 beamline of Shanghai Synchrotron Radiation Facility (SSRF) and 1W1B beamline of Beijing Synchrotron Radiation Facility (BSRF). A fixed-exit double-crystal Si (111) monochromator was used for energy selection. The spectra were analyzed using Athena and Artemis [26]. The Fourier transformation of the k^2-weighted extended X-ray absorption fine structures (EXAFS) oscillations, $k^2 \cdot \chi(k)$, from *k* space to *R* space was performed over a range of 3.0-12.0 $Å^{-1}$ to obtain a radial distribution function. And the wavelet transform (WT) analysis was based on Morlet wavelets with optimum resolution.

2.3. Catalytic tests

The FTS performance was evaluated on a fixed-bed reactor. Typically, 0.5 g catalyst (pellet size: 0.25 − 0.42 mm) was loaded in the stainless tube (*i.d.* 8 mm) and then pre-reduced in H_2 flow (40 mL min^{-1}, ambient pressure) at 300 °C for 3 h. The reduced catalyst was named as the Ru/TiO_2-*T*-H catalyst. After the reactor was cooled down to room temperature, the reaction was carried out at 220 °C in syngas (2.0 MPa, 4800 L kg_{cat}^{-1} h^{-1}, H_2/CO = 2, and 1.5 % N_2 internal standard). The products in the gas phase were detected by an online gas chromatograph (GC) equipped with thermal conductivity detector (TCD) and flame ionization detector (FID), whereas the liquid products were tested by an offline GC with FID detectors. CO conversion, product selectivity, Ru time yield and TOF were defined by the following equations.

$$X_{CO} = \frac{n_{CO,\,inlet} - n_{CO,\,outlet}}{n_{CO,\,inlet}} \times 100\% \quad (1)$$

$$S_{C_n} = \frac{nF_{C_n}}{\sum_{n=1}^{N} nF_{C_n}} \times 100\% \quad (2)$$

$$\text{Ru time yield} = \frac{n_{CO,\,inlet} - n_{CO,\,outlet}}{n_{Ru} \times t} \quad (3)$$

$$TOF_{exp} = \frac{n_{CO,\,inlet} - n_{CO,\,outlet}}{n_{Ru} \times D_{H_2\text{-TPD}} \times t} \quad (4)$$

In Eq. (1), X_{CO} means the conversion of CO. $n_{CO,\ inlet}$ and $n_{CO,\ outlet}$ means the moles of CO in the reactants and products, respectively. S_{Cn} in Eq. (2) is the selectivity of hydrocarbons in different carbon number, in which *n* means the carbon numbers. F_{Cn} represents the molar of hydrocarbon with the *n* carbon atoms. Traces of CO_2 (< 3%) were excluded here. In Eqs. (3) and (4), n_{Ru} represents the Ru° moles in the reaction. $D_{H2\text{-TPD}}$ is the dispersion calculated according to the H_2-uptake value [5] and *t* is the reaction time. Carbon balances were beyond 90 % for all tests. The activity and selectivity were calculated for a duration of 24 h after 3 h on steam at a steady state.

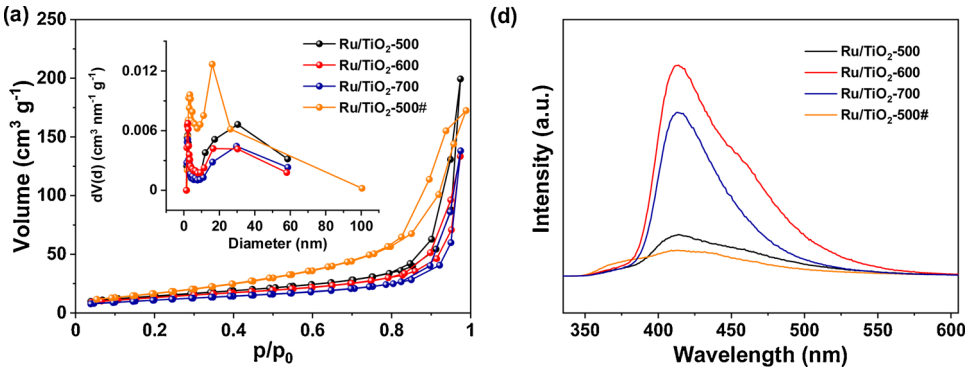

Fig. 1. Structural characterization of the Ru/TiO_2-*T* catalysts: (a) N_2 adsorption-desorption isotherms, the inlet shows the pore distribution; and (b) PL spectra.

Table 1
Physical and chemical properties of the as-prepared Ru/TiO_2 catalysts.

Catalysts	$d_{reduced}$[a] nm	d_{spent}[a]	S_{BET} m^2 g^{-1}	V_{pore} cm^3 g^{-1}	f_A[b]	Ru/Ti ratio[c]
Ru/TiO_2-500	3.1	3.6	52.1	0.16	0.96	0.154
Ru/TiO_2-600	3.3	4.2	47.3	0.12	0.95	0.125
Ru/TiO_2-700	3.4	5.9	41.3	0.10	0.89	0.075
Ru/TiO_2-500#	3.5	4.3	59.5	0.22	0.98	0.151

[a] Particle size of Ru NPs determined by TEM.
[b] The weight ratio of anatase determined by XRD.
[c] Ru/Ti atomic ratio determined by XPS.

3. Results and discussion

3.1. Catalyst characterization of Ru/TiO_2

The N_2-sorption results in Fig. S1 and 1 (a) suggests that the pore structure of the Ru/TiO_2 catalysts is maintained during the whole DA-modified preparation process [21]. As shown in Table S1, the specific surface area and pore volume of Ru/TiO_2@DA increased, indicating the formation of porous dopamine shell covering on the whole catalysts. Compared with the N_2-isotherms of Ru/TiO_2-*T* catalysts in Fig. 1(a), Ru/TiO_2-500 shows a similar pore structure to Ru/TiO_2, proving that the shell has been successfully removed. After removing the carbon shell, all of the Ru/TiO2-*T* catalysts experienced a slight decrease in the surface area with the increased calcination temperatures, as listed in Table 1. The PL spectra in Figs. S2 and 1 (b) demonstrated the successful coating and removal of dopamine and carbon shell in the synthesis process, which is consistent with the TG (Fig. S3), TEM (Fig. S4) and Raman (Fig. S5) results in the supporting information.

Fig. 2 shows the H_2-TPR profiles of the Ru/TiO_2 catalysts. Generally, the peaks at 200 − 300 °C are attributed to the reduction of bulk RuO_2 to metallic Ru, while the peaks at lower temperatures are assigned to the reduction of highly dispersed RuO_x with weaker Ru–support interaction [11,27–30]. In Fig. 2, all of the catalysts have a broad reduction peak centered at around 219 °C, and the profile variation in the range of 100 − 300 °C of these catalysts was similar, especially for Ru/TiO_2-500 and Ru/TiO_2-600. It indicated that the reducibility of highly dispersed RuO_x species on these catalysts was comparable [31]. According to the reduction behavior of the catalysts, 300 °C was chosen as the pre-treatment temperature for H_2 reduction prior to the activity tests.

The crystal structure of Ru/TiO_2 catalysts was characterized by XRD. As shown in Fig. S6, anatase was confirmed as the predominant phase in commercial TiO_2 (P25) [21,32], and no distinct changes in the crystal phase of TiO_2 occurred during the synthetic steps. The XRD results in Fig. 3(a) and (b) indicates that the Ru/TiO_2-*T* catalysts consist of the two type TiO_2 phases (anatase and rutile) and RuO_2 phase. It is noteworthy that the peak intensity of rutile in Ru/TiO_2-500# in Fig. 3(b) was lower than other fresh catalysts, which could be ascribed to the difference in the calcination conditions. The 700 °C calcination in N_2 in Ru/TiO_2-*T* would lead to the increase in the crystallinity and XRD peak intensity of rutile. To further determine the degree of the crystal phase transformation of TiO_2 occurred during the calcination in air, the weight ratio of anatase (f_A) was calculated by the following equation [33,34]: $f_A = (1 + 1.26\, I_R/I_A)^{-1}$. Where I_R and I_A mean the intensities of rutile (101) and anatase (110) peaks in the XRD patterns, respectively. As shown in Table 1, Ru/TiO_2-500# has the highest f_A and corresponding less intensity of rutile, which could be ascribed to the lack of calcination in N_2 at 700 °C. While for other catalysts, the crystal transformation from anatase to rutile appeared at 700 °C and f_A decreased with increasing calcination temperatures. This difference in the phase composition of the support might lead to the changes in the FTS catalytic performance. Hence, the calcination temperature range below 600 °C is acceptable to exclude the influence of the support.

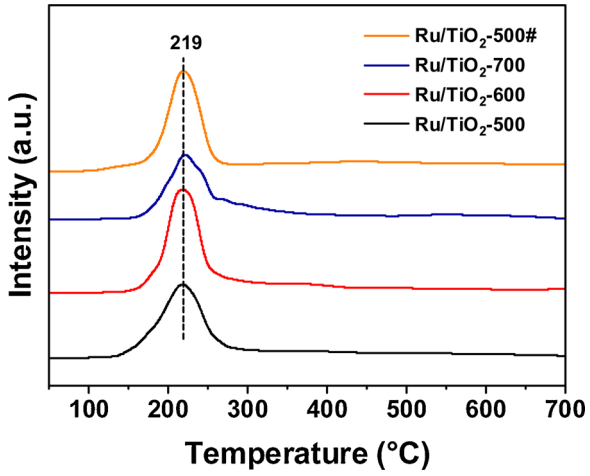

Fig. 2. H_2-TPR profiles of the Ru/TiO_2 catalysts.

Fig. 3(c) and (d) show the XRD patterns of the reduced catalysts. The diffraction peak corresponding to the RuO_2 phase in Fig. 3(b) has disappeared in comparison with the patterns in Fig. 3(d), indicating that the bulk RuO_2 have been reduced and 300 °C is suitable for the reduction of RuO_2. Notably, characteristic peaks of metallic Ru (Ru°) were not detected in Fig. 3(c), which might be ascribed to the high dispersion of Ru NPs, whose particle size was below the detection limit of XRD [31]. Fig. 4 shows the TEM images of the reduced catalysts and the metallic Ru NPs has been indicated in the dashed circles. The corresponding particle size distribution of Ru NPs in all catalysts clearly demonstrates that the size of Ru NPs on the catalysts is around 3 nm, which is consistent with the size range of undetectable Ru° species in the above XRD results.

The chemical states of Ru species were analyzed through the XAFS studies of the reduced catalysts at the Ru *K*-edge. As shown in the XANES spectra (Fig. 5(a)), the absorption thresholds of the reduced catalysts located close to that of Ru foil, indicating that Ru species mainly exist in the metallic state. In the Fourier transformed k^3-weighted EXAFS spectra (Fig. 5(b)), the curves of the catalysts have a main peak at 2.35 Å, corresponding to the metallic Ru-Ru scattering peak [35,36]. The absence of the Ru-O bond at about 1.48 Å excludes the presence of bulk Ru oxides in these reduced catalysts [23]. To further demonstrate the reduction of RuO_2 NPs, we analyzed wavelet transform (WT) of Ru *K*-edge EXAFS of the reduced catalysts. In Fig. 5(c), the WT contour plots of Ru/TiO_2-500-H show only one intensity maximum at 9.1 $Å^{-1}$, corresponding to Ru-Ru coordination. Additionally, no intensity maximum related to Ru-O contribution was observed at lower coordination shells compared with the WT plot of RuO_2 in Fig. 5(g), coinciding with the above XANES and XRD results.

To further determine the coordination numbers (CN) and interatomic Ru-Ru distances of the reduced catalysts, the fitting results of EXAFS analysis were given in Table 2 and Fig. 6. The first coordination shell of Ru-Ru located at around 2.68 Å in Ru/TiO_2-500-H and Ru/TiO_2-*T*-H had the similar coordination number. This finding indicates the similar local coordination environment of these reduced catalysts, and slightly enlarged Ru NPs with the increased calcination temperatures, which was consistent with the TEM results in Fig. 4.

The amount of chemisorbed hydrogen of the catalysts was measured through the H_2-TPD method, and the dispersion and accessible surface area of metallic Ru were calculated based on the values of H_2-uptake in Table 3. Ru/TiO_2-500-H exhibited the maximum H_2-uptake and hence showed the largest Ru surface area and dispersion. For the Ru/TiO_2 catalysts having experienced DA sacrificial coating strategy, the higher annealing temperature led to the greater blockage of the exposed-Ru metal surface, and the lower Ru dispersion. While for Ru/TiO_2-500#-H, it exhibited the significantly smaller H_2-uptake, Ru surface area and

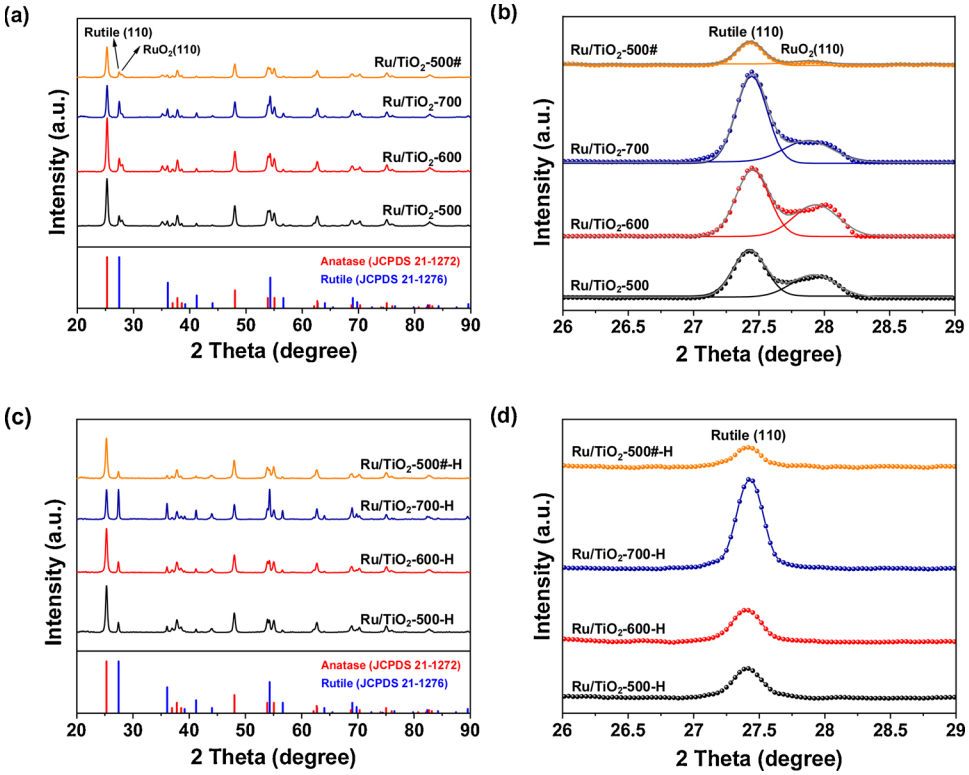

Fig. 3. Structural characterization of the catalysts: (a, c) full XRD patterns and (b, d) XRD patterns in the 2 theta range of 26-29 degrees; (a, b) fresh and (c, d) reduced catalysts.

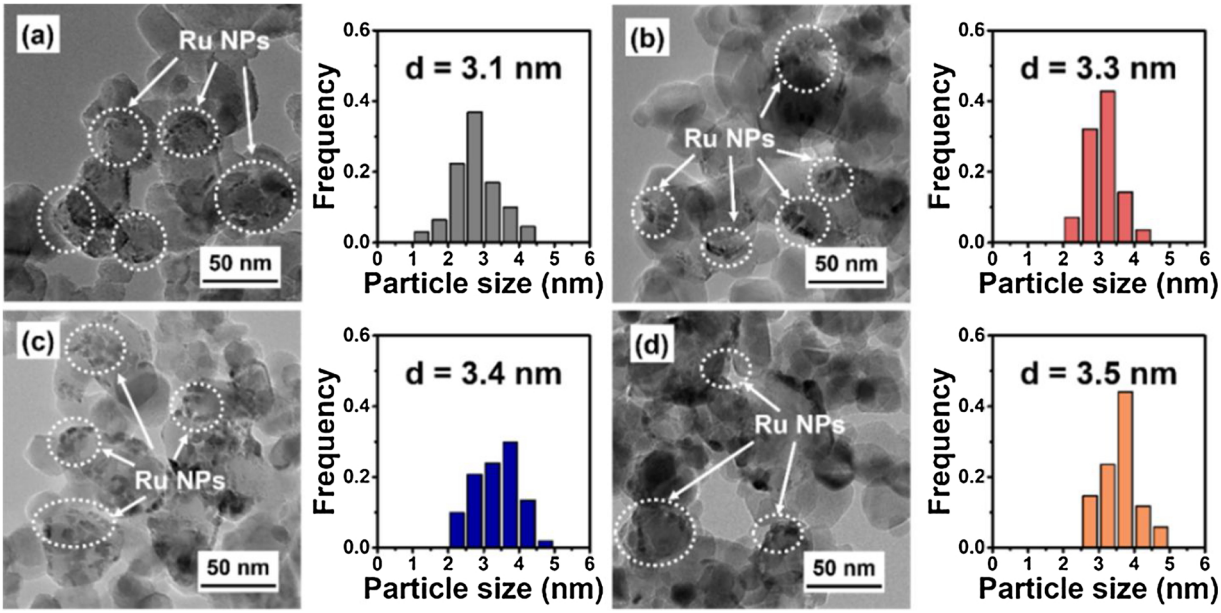

Fig. 4. TEM images of the reduced catalysts: (a) Ru/TiO_2-500-H, (b) Ru/TiO_2-600-H, (c) Ru/TiO_2-700-H, and (d) Ru/TiO_2-500#-H.

dispersion compared with the Ru/TiO_2-*T*-H catalysts, indicating the serious encapsulation of TiO_x species on Ru NPs therein.

The Ru/Ti atomic ratio could reflect the relative amount of the surface Ru atoms [37], and the values on the reduced catalyst surface were obtained from the in situ XPS results (Fig. 7 and Table 3). Considering the effect of different calcination temperatures on the structural rearrangement of metal NPs, we mainly compared Ru/TiO_2-500-H and Ru/TiO_2-500#-H, which experienced the same thermal treatment. It is of great interest to note that the DA sacrificial coating strategy could successfully suppress the encapsulation of Ru NPs by TiO_x fragments, as evidenced by the high surface Ru/Ti ratio of Ru/TiO_2-500-H (0.142). However, this value of Ru/TiO_2-500#-H decreased to 0.047 beyond the margin of error. This further provides the convincing evidence for the increased TiO_x coverage on Ru NPs by directly heating catalysts in the oxidative atmosphere, which led to the promoted formation of inaccessible Ru sites.

To further certify this conclusion, we performed XPS analysis of the fresh catalysts. As given in Table 1, the Ru/Ti ratio of the fresh catalysts was similar except for the Ru/TiO_2-700, which might be attributed to the high annealing temperature and the phase transformation of the

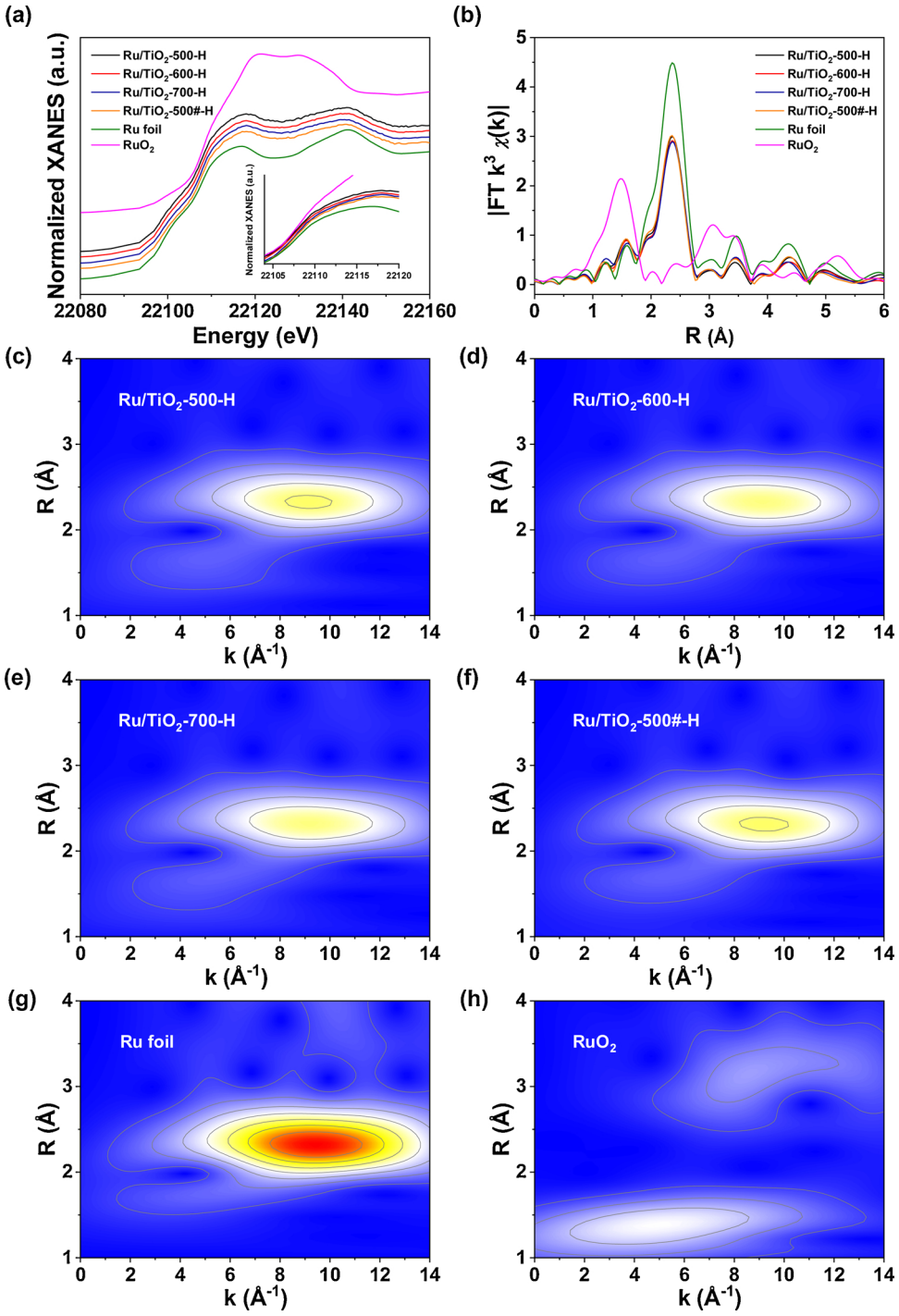

Fig. 5. (a) XANES spectra; (b) Fourier transformed (FT) k^3-weighted χ(k)-function of the EXAFS spectra for Ru K-edge; (c-h) Wavelet transform (WT) for Ru K-edge of the reduced catalysts, Ru foil and RuO_2.

support. Especially, Ru/TiO_2-500 and Ru/TiO_2-500# without H_2 reduction had the similar Ru/Ti ratio of ~0.15. This phenomenon proved that for Ru/TiO_2-500#-H the support encapsulation on metal NPs mainly occurred during the H_2 reduction procedure at 300 °C, rather than the heat treatment under the oxidative environment.

Deconvolution was used to testify the details of Ru species since the XPS spectra of both C 1*s* and Ru 3*d* in the region of 279 − 287 eV are totally overlapped. The binding energy values at 280.2–282.4 eV and 284.2–284.4 eV could be attributed to the Ru $3d_{5/2}$ and Ru $3d_{3/2}$ of metallic Ru [38]. The Ru 3*d* peaks at 281.2–281.5 eV (green region) could be ascribed to the positively charged Ru species ($Ru^{\delta+}$), which is the inevitable consequence of SMSI [39]. Notably, all Ru binding energy peaks of the Ru/TiO_2-500/600/700-H catalysts show the negative shift when compared with Ru/TiO_2-500#-H, indicating that the DA sacrificial coating on the catalysts can strengthen the electron transfer from the TiO_2 support to Ru NPs [40,41].

The schematic overview of the pretreatments applied to the Ru/TiO_2 catalysts was briefly depicted in Scheme 1. As mentioned before, the DA coating offered a rigid shell for both the metal NPs and the support of the Ru/TiO_2-*T*-H catalysts during the thermal treatment, which avoids the encapsulation of Ru NPs by TiO_x overlayer during the H_2 reduction treatment. For example, Ru/TiO_2-500-H and Ru/TiO_2-500

Table 2
Structural parameters of the reduced catalysts and Ru foil extracted from the EXAFS fitting.

Catalysts	Scattering path	*CN*[a]	*R* (Å)[b]	σ^2 (10^{-3} Å^2) [c]	*R* factor[d]
Ru/TiO_2-500-H	Ru-Ru	9.8	2.67 ± 0.01	4.45 ± 0.34	0.0132
Ru/TiO_2-600-H	Ru-Ru	9.9	2.68 ± 0.01	4.39 ± 0.27	0.0058
Ru/TiO_2-700-H	Ru-Ru	10.8	2.68 ± 0.01	5.11 ± 0.38	0.0100
Ru/TiO_2-500#-H	Ru-Ru	10.5	2.67 ± 0.01	4.78 ± 0.35	0.0121
Ru foil	Ru-Ru	12.0*	2.68 ± 0.01	3.20 ± 0.23	0.0130

[a] *CN* is the coordination number.
[b] *R* is interatomic distance.
[c] σ^2 is Debye-Waller factor; [d]*R* factor is used to evaluate the goodness of the fitting.
* This value was fixed during the EXAFS fitting, based on the known structure of Ru foil [30].

had the similar Ru/Ti ratio of ~ 0.15, as evidenced by the XPS results in Tables 1 and 3. Contrarily, Ru NPs on Ru/TiO_2-500#-H were seriously covered by TiO_x layer, since its Ru/Ti ratio (0.047) greatly dropped, compared with Ru/TiO_2-500# (0.151). Similar results are also achieved by the H_2 chemical adsorption experiments in Table 3. Herein, the encapsulated structure could not be clearly observed in the high-resolution TEM images in Fig. 4 due to the low contrast between Ru NPs and TiO_2. Additionally, the pancake-like shape of metal particles also brings the difficulty to direct observation of support encapsulation.

3.2. Fischer-Tropsch synthesis performance

Fig. 8 and Table S2 gives the FTS activity and selectivity of the reduced catalysts. It is notable that the Ru time yield of Ru/TiO_2-500-H were the highest, whereas Ru/TiO_2-700-H showed the lowest catalytic performance. The apparent activation energies (E_{app}^{act}) of all catalysts were obtained from the Arrhenius plots, with the CO conversion (X_{CO}) lower than 20 % (Fig. 9). The E_{app}^{act} of Ru/TiO_2-500-H is 83.3 kJ mol^{-1}, within the reported data range of 67 − 155 kJ mol^{-1} on Ru-based catalysts [42]. The E_{app}^{act} value follows the sequence of Ru/TiO_2-700-H > Ru/TiO_2-600-H > Ru/TiO_2-500#-H > Ru/TiO_2-500-H, while the Ru time yield is in a reverse trend. In addition, the Ru time yield of Ru/TiO_2-500-H was even higher than that of the previously reported Ru-based FTS catalysts [4–6,24,43], as summarized in Table S2. When compared with the cobalt- [44–47] and iron-based [48] catalysts in FTS under comparable reaction conditions in the reported references, the Ru/TiO_2-500-H also exhibited excellent FTS performance. As for the product distribution (Table S2), Ru/TiO_2-500-H showed a higher selectivity towards C_{5+} hydrocarbons and a lower selectivity towards CH_4 than other catalysts. Nevertheless, Ru/TiO_2-500#-H has the lowest selectivity towards C_{5+} products and the highest selectivity towards CH_4 among the catalysts, although it has a higher activity than Ru/TiO_2-600-H and Ru/TiO_2-700-H.

Fig. 10 shows the catalytic stability of the catalysts. The CO conversion of Ru/TiO_2-500-H kept stable in a 160 -h reaction, while the activity of Ru/TiO_2-700-H dropped quickly. The CO conversion of Ru/TiO_2-600-H decreased slightly, while that of Ru/TiO_2-500#-H declined about 7 % of the initial CO conversion. The deactivation of the catalysts might result from carbon deposition and/or metal NPs sintering [49–52]. The TG curves of the spent catalysts are presented in Fig. S7. The weight loss before 150 °C could be attributed to the removal of water, and the combustion of FTS hydrocarbons appeared above 200 °C [53]. The weight loss of the Ru/TiO_2-*T*-H catalysts is quite similar in the range of 22–27 %. It suggests that the deactivation of the catalysts was not determined by carbon deposition. However, in Fig. 11, the size of Ru NPs increased for all of the spent catalysts, especially for Ru/TiO_2-700-H. It indicates that the deactivation mainly results from the sintering of Ru NPs.

3.3. Analysis of active sites through in situ DRIFTS characterization

Catalytic reactions are generally considered to occur on specific active sites on the surface, and the intrinsic activity on a per site (i.e., TOF) provides a fair measure to compare catalysts with different compositions and properties [54]. However, in most cases, TOF is mainly calculated based on the assumption that all the active sites on a catalyst are equally active or only one kind of active site contributes to the catalytic activity. This assumption excludes the actual existed varieties in the activities and site types, which may bring misunderstanding for many structure-sensitive or site-specific reactions [22]. As discussed above, many studies clarified the active sites of FTS simply basing on the in situ characterization results under ambient conditions [9,53], including theoretical calculations as well [55]. Unfortunately, they are quite different from real operations conducting at high pressures and temperatures. The gap between them gives rise to uncertainties and ambiguities regarding the identification of the intrinsic active sites. Thus, it is urgent to employ in situ characterization methods operated under real reaction conditions to get consensus on the impact of active site types on FTS performance, and to reveal intrinsic mechanisms.

To solve this problem, the in situ DRIFTS studies were conducted to investigate the adsorption behavior of CO on Ru sites under the real reaction conditions, as described in procedure A in the experimental section. In Fig. 12, the spectra show bands at frequencies of 2135, 2067 and 1970 cm^{-1}, which were attributed to CO species adsorbed on different Ru sites. Normally, the band at 2135 cm^{-1} could be attributed to multicarbonyl species adsorbed on partially oxidized $Ru^{\delta+}$ sites (donated as $Ru^{\delta+}(CO)_x$ with x = 2 or 3) [56,57]. The $Ru^{\delta+}$ sites mainly originate from their strong interactions with the TiO_2 support and CO-induced oxidative disruptive process with the participation of hydroxyl from the support [29,57]. The second band at 2040 − 2067 cm^{-1} appears at the vibrational frequencies where CO species linearly adsorbed on surface-exposed reduced Ru crystallites (Ru − CO) [57–59]. The third broad band locates in the range of 2025 − 1800 cm^{-1}, and is centered at around 1970 cm^{-1}, which might be ascribed to the linear-adsorbed CO on the boundary between the metal particles and the support [57] or bridge-adsorbed CO on metal sites [53,60]. The bridge-type CO adsorption is known to be more favored on extended surfaces (e.g. terraces) of large metal crystallites, and the band of which on Ru catalysts generally locates at frequencies below 1800 cm^{-1} [57,60,61]. It should be noticed that the size of Ru NPs on the Ru/TiO_2 catalysts in this study is around 3 nm, which is too small to be suitable for bridged − CO adsorption. Especially, this band locates above 1800 cm^{-1}. Thus, we propose here that the band centered at 1970 cm^{-1} could be assigned to CO linearly adsorbed on interfacial Ru sites strongly interacting with the TiO_2 support, denoted as (TiO_2)Ru − CO [57].

In FTS, metallic Ru sites are active for CO hydrogenation, and herein, there are two kinds of active sites, that is, surface-exposed Ru sites (denoted as Ru_E) and interfacial Ru sites (denoted as Ru_I) on our catalysts [3]. Since only Ru/TiO_2-500-H exhibited a weak shoulder peak at 2040 cm^{-1}, we chose the band locating at 2067 cm^{-1} for our calculation [62–64]. As shown in Fig. 12, Ru/TiO_2-600-H has a lower peak intensity of Ru − CO on Ru_E than that of (TiO_2)Ru − CO on Ru_I.

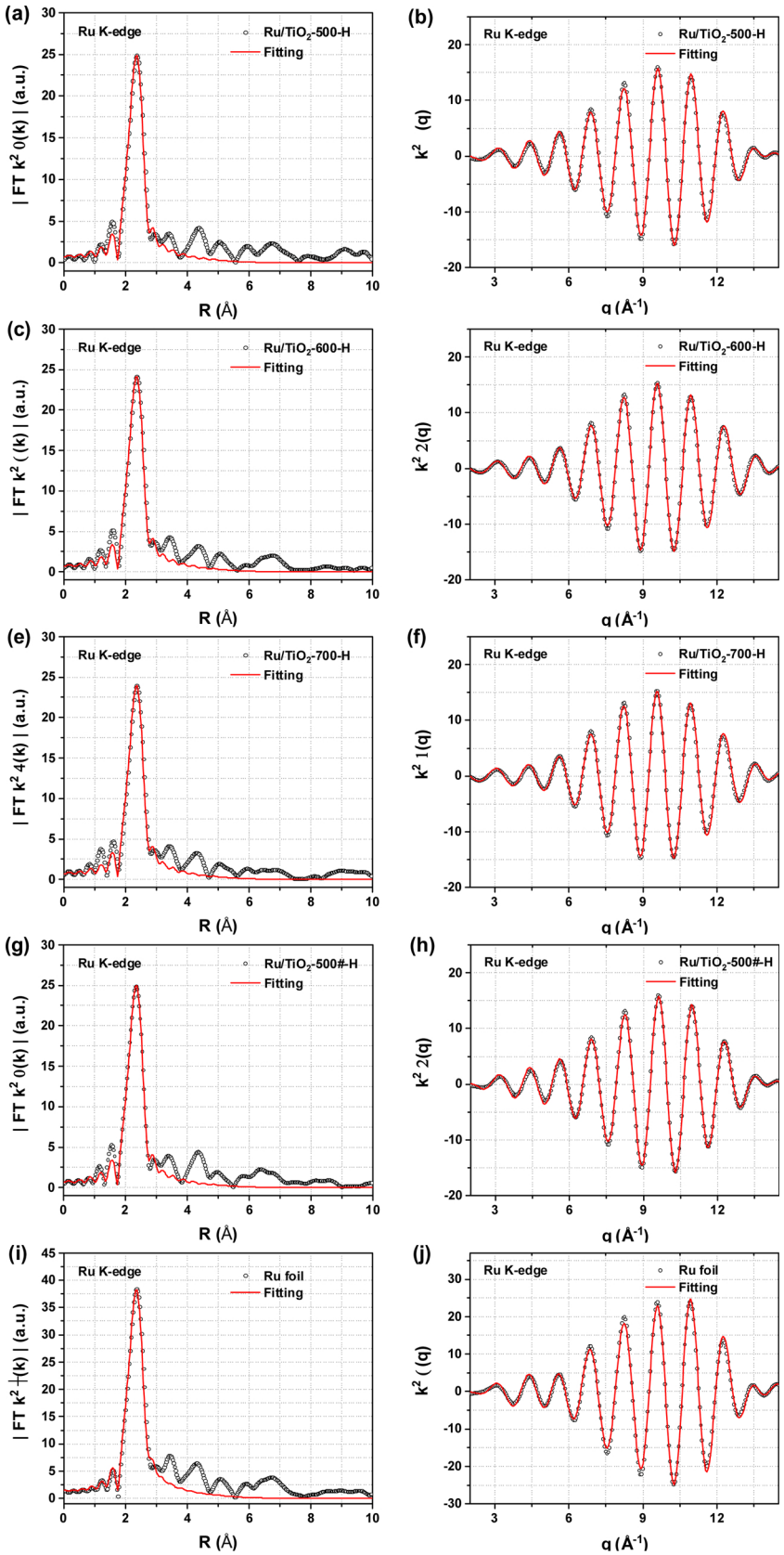

Fig. 6. R space and inverse FT-EXAFS fitting results: (a, b) Ru/TiO_2-500-H, (c, d) Ru/TiO_2-600-H, (e, f) Ru/TiO_2-700-H, (g, h) Ru/TiO_2-500#-H, and (i, j) Ru foil.

However, Ru/TiO_2-500-H exhibits the opposite regulation, although the two catalysts were synthesized with the same method, except for the calcination temperatures. Generally, integrated absorbance in IR spectra is linked to quantities of surface adsorbed CO on active sites. Accordingly, the difference in the apparent activity in Fig. 8 should be directly linked to both the number and intrinsic activity of the Ru_E and

Table 3
Physical properties of the reduced Ru/TiO_2 catalysts.

Catalysts	H_2-uptake[a] μmol H_2 g_{Ru}^{-1}	Dispersion[a]%	Ru surface area[a] m^2 g_{Ru}^{-1}	Ru/Ti ratio[b]
Ru/TiO_2-500-H	2262	45.7	222.7	0.142
Ru/TiO_2-600-H	2021	40.9	198.9	0.096
Ru/TiO_2-700-H	1509	30.5	148.5	0.051
Ru/TiO_2-500#-H	1425	28.8	140.2	0.049

[a] Determined by H_2-TPD results.
[b] Determined by in situ XPS analysis.

Ru_I sites on the catalysts. According to the previous studies, we assume that the proportionality factors between integrated absorbance and surface concentration are the same for linear-adsorbed CO on both Ru_E and Ru_I [65,66]. Based on the corresponding peak areas in the DRIFTS spectra, the ratio of the two sites on Ru/TiO_2-500-H and Ru/TiO_2-600-H was given in Table 4. In addition, it is well recognized that Ru-catalyzed FTS is a structure-sensitive reaction, which means the TOF might change with the Ru NPs size [67]. In Fig. 4, the Ru NPs size of those reduced catalysts was similar, so the size effect on the reactivity could be ignored in this work. In Fig. 12, it is of interest to note that the frequencies of the bands at 2067 and 1970 cm^{-1} of Ru/TiO_2-500-H and Ru/TiO_2-600-H, corresponding to Ru_E and Ru_I sites, respectively, are the same when compared with other catalysts. It demonstrates the similar activity of Ru_E/Ru_I sites for Ru/TiO_2-500-H and Ru/TiO_2-600-H. It provides the possibility to clarify the intrinsic activity of the Ru_E and Ru_I sites for further recognition of the FTS mechanism by deep analysis of the two catalysts.

The experimental TOF (TOF_{exp}) value of the two catalysts and TOF for two sites were also given in Table 4. Here, we denote the TOF of Ru_E sites and Ru_I sites as TOF_E and TOF_I, respectively. Considering both sites adsorbed linear CO species, it is reasonable to assume that the adsorption mode for these two sites exhibited the same molar extinction coefficient. Hence, the TOF_E and TOF_I could be quantified after combination with the experimental TOF values through the equation of $TOF_{exp} = \frac{TOF_E \times n_E + TOF_I \times n_I}{n_E + n_I}$. Here, TOF_{exp} is the experimental TOF value, and n_E and n_I are the site number of Ru_E and Ru_I, respectively. The site number was calculated based on the Ru surface area in Table 3 and the surface density (1.5×10^{19} atoms m^{-2}) [53,68]. As a result, TOF_E (250.9×10^{-3} s^{-1}) is around 5.3-fold TOF_I (47.2×10^{-3} s^{-1}) for Ru/TiO_2-500-H and Ru/TiO_2-600-H. Thus, we can conclude that the activity of surface-exposed Ru sites is much higher than that of interfacial Ru sites. Besides, compared with other catalysts, the adsorbed CO stretching frequency for Ru/TiO_2-500#-H exhibited a red shift for $(TiO_2)Ru-CO$ species. This could be ascribed to the discrepancies in electronic properties among these catalysts, which is consistent with the above XPS results.

To get a deep insight into the thermal stability of various CO adsorbed species, the in situ DRIFTS spectra were collected at elevated temperatures in He flow after CO adsorption at 2.0 MPa and 50 °C. As shown in Figs. 13 and S8, the intensities of all adsorbed CO bands weakened with the increased temperatures for all of the Ru/TiO_2-*T*-H catalysts, indicating the thermal desorption of adsorbed CO species. Especially, the band centered at 1975 cm^{-1} decreased sharply even at the temperature below 100 °C, indicating that CO species adsorbed on interfacial Ru sites were quite thermally unstable. Nevertheless, the band attributed to CO adsorbed on surface-exposed Ru sites was more thermally stable and decreased slowly even at temperatures above 180 °C, which is consistent with the results of Kondarides et al. [57,69].

Interestingly, the catalysts show quite different CO adsorption behavior at the low and high adsorption temperatures in Figs. 12, 13 and

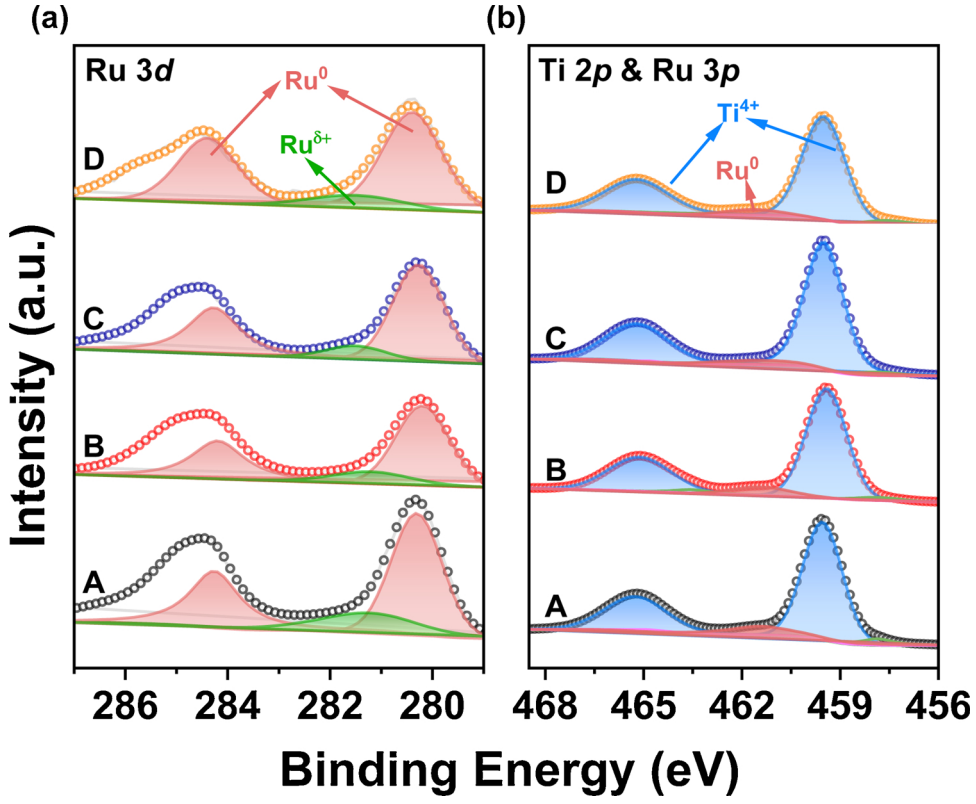

Fig. 7. In situ XPS spectra of (a) Ru 3*d* and (b) Ti 2*p* spectra of the reduced catalysts: (A) Ru/TiO_2-500-H, (B) Ru/TiO_2-600-H, (C) Ru/TiO_2-700-H and (D) Ru/TiO_2-500#-H.

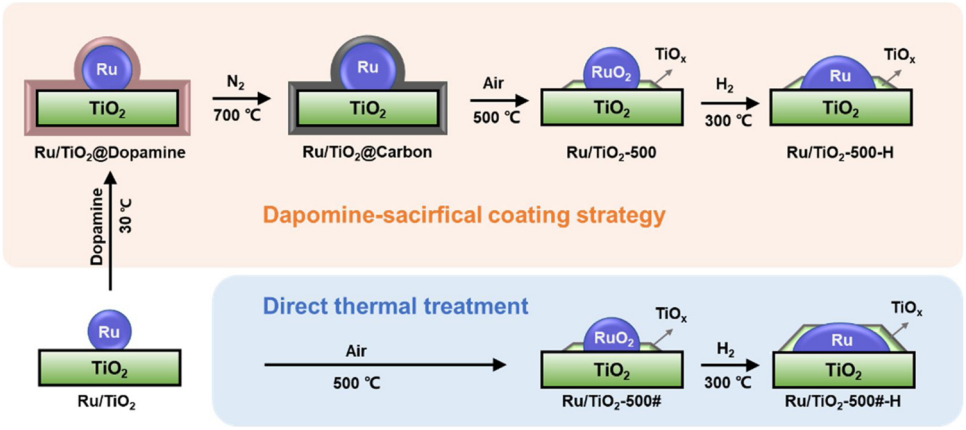

Scheme 1. Schematic overview of the pretreatments applied to the Ru/TiO_2 catalysts.

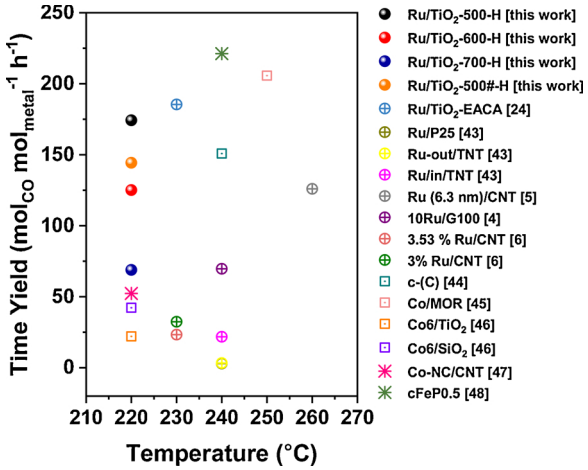

Fig. 8. Activity of catalysts in FTS normalized to the total metal amount at different reaction temperatures: Ru-based catalysts were marked as circle; Co-based catalysts were marked as square and Fe-based catalysts were marked as star.

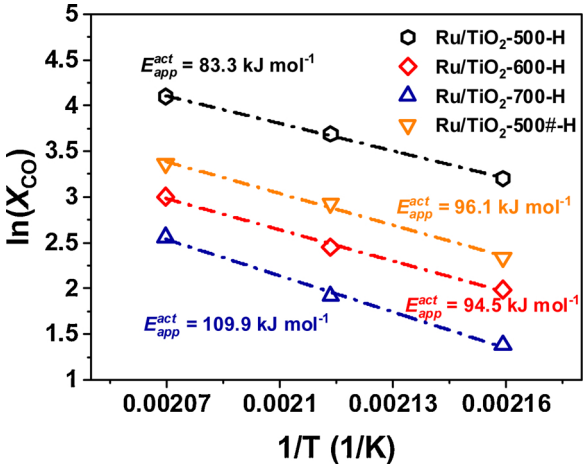

Fig. 9. Arrhenius plots of the as-prepared catalysts.

S8. In Fig. 13(a), when CO was pre-adsorbed at 50 °C, the CO coverage on Ru_E was much lower than that at 220 °C, especially for Ru/TiO_2-500-H. However, for the spectra collected at the CO adsorption temperature of 220 °C in Fig. 12, the band intensity of CO adsorption on Ru_E sites is even stronger than that on Ru_I sites. The only difference in Figs. 12 and 13 is the initial CO adsorption temperature, that is, 220 and 50 °C,

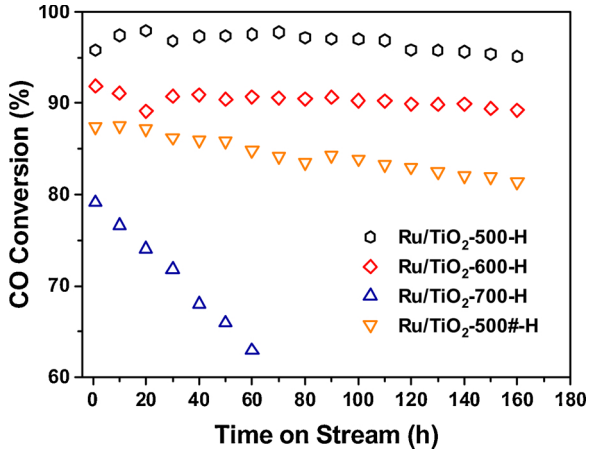

Fig. 10. Stability tests of the catalysts.

respectively. This strange phenomenon might be explained by the competitive adsorption behavior of different adsorbed CO species. At the low temperatures like 50 °C, CO species adsorbed easier on Ru_I sites to get much stronger band intensity than that on Ru_E sites. However, at the high temperatures like 220 °C, $(TiO_2)Ru-CO$ species on Ru_I are thermally unstable, as evidenced in Fig. 13, and accordingly thermally stable CO species on Ru_E become dominant to involve in FTS reactions in Fig. 12. Apparently, in this work, the in situ DRIFTS experiments operated at the high temperatures and pressures could fill the gap between the realistic reaction and ambient experimental conditions, offering the comprehensive understanding of the intrinsic mechanism in FTS processes.

In Fig. 14, the reduced Ru/TiO_2-500-H and Ru/TiO_2-500#-H catalysts were exposed to the real reaction conditions for 0.5 h to reach the steady-state (see procedure C in Experimental Section). Because the bands in the region of 1900-2200 cm^{-1} are obscured by gaseous CO, only the spectra in the region of $2700-3050$ cm^{-1} are presented and discussed here [70,71]. The characteristic bands of adsorbed CH_x species can be clearly observed in Fig. 14, indicating that the C–C coupling occurs after the syngas adsorption under the operating conditions. The sharp peak at 3015 cm^{-1} accompanied by the *P* and *R* branch fine structure could be ascribed to the rocking vibration of gaseous CH_4 [70,72], which was generated in a large quantity under the reaction conditions. According to the previous report, the intensity of this peak is directly relevant to the catalytic activity of FTS catalysts [70]. Ru/TiO_2-500-H has a stronger band at 3015 cm^{-1} than Ru/TiO_2-500#-H, indicating that the former has a higher FTS activity, which is consistent with the activity results in Fig. 8. The band of methyl ($-CH_3$) group located at 2966 cm^{-1} and the bands at 2929 and 2857 cm^{-1} are

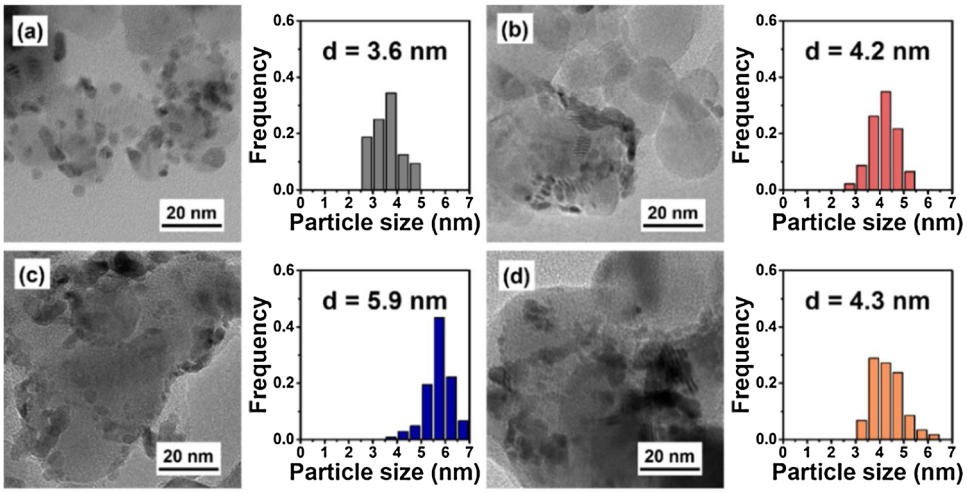

Fig. 11. TEM images of the spent catalysts: (a) Ru/TiO_2-500-H, (b) Ru/TiO_2-600-H, (c) Ru/TiO_2-700-H, and (d) Ru/TiO_2-500#-H.

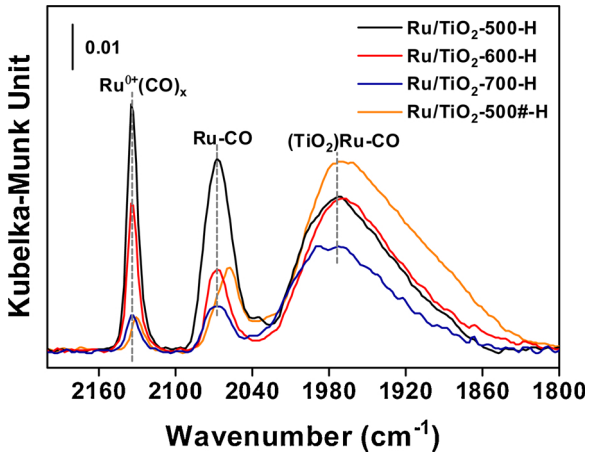

Fig. 12. In situ DRIFTS spectra of CO adsorption at 2.0 MPa and 220 °C.

Table 4
Ratio of Ru_I/Ru_E and TOF values for the reduced Ru/TiO_2 catalysts.

Catalysts	Ratio of Ru_I/Ru_E	TOF (10^{-3} s^{-1})		
		TOF_{exp}	TOF_I	TOF_E
Ru/TiO_2-500-H	2.4	105.3	47.2	250.9
Ru/TiO_2-600-H	7.3	84.8	47.2	250.9

ascribed to stretching vibrations of methylene (−CH_2-) groups of alkanes [72,73]. The intensity of those bands in the C–H stretching region follows the same tendency with the band at 3015 cm^{-1}, suggesting the higher activity of Ru/TiO_2-500-H for CO hydrogenation.

After the 0.5 h reaction, the pressure was dropped to ambient pressure, and He flow was introduced to investigate the thermal stability of the generated CH_x intermediate species. The CH_x bands on Ru/TiO_2-500-H are much stronger than those of Ru/TiO_2-500#-H, coinciding with the enhanced chain growth ability and the higher selectivity towards longer hydrocarbons of Ru/TiO_2-500-H. Additionally, the band ascribed to -CH_2- species of Ru/TiO_2-500-H (2930 cm^{-1}) exhibits the redshift compared with Ru/TiO_2-500#-H (2933 cm^{-1}), suggesting the stronger metal–C* bond on the former catalyst under the realistic reaction conditions [74–76]. The stable adsorption of C* species on Ru° is beneficial to the CC— coupling reaction stimulating chain growth to produce heavy hydrocarbons. Thus, Ru/TiO_2-500-H exhibits the lower CH_4 selectivity compared with other Ru/TiO_2-*T*-H catalysts and the reported Ru-based FTS catalysts in Table S2 [5,43,77].

4. Conclusions

Herein, we employed the DA sacrificial coating strategy to prepare the Ru/TiO_2-*T*-H catalysts with well-distributed Ru NPs (~ 3 nm). Systematic characterizations revealed that the DA-derived carbon shells could form a complete coating on the catalysts, which can efficiently isolate Ru NPs and TiO_2 during the annealing process and hence suppress the encapsulation of metal NPs by the TiO_2 support in the H_2 reduction procedure. Subsequently, the Ru surface area and the site number increased significantly, especially for the number of the surface-exposed sites. The Ru/TiO_2-500-H catalyst with the maximum site number hence exhibited the highest apparent activity in FTS. By combining the experimental TOF values and in situ DRIFTS results, we first discovered that the TOF of surface-exposed Ru sites is qualitative 5.3-fold that of interfacial Ru sites in Ru/TiO_2-500-H and Ru/TiO_2-600-H. The DA sacrificial coating strategy employed here prevented Ru NPs from sintering, and Ru/TiO_2-500-H exhibited the excellent catalytic stability in 160 h. Additionally, our findings indicate that the strong bond between Ru sites and CH_x intermediates on Ru/TiO_2-500-H facilitates the chain growth to achieve the high selectivity towards heavy products and lower the CH_4 selectivity.

Declaration of Competing Interest

The authors declare that they have no known competing financial interests or personal relationships that could have appeared to influence the work reported in this paper.

Acknowledgements

This work is financially supported by the National Natural Science Foundation of China (No. 21676182; 21476159), the Program for Introducing Talents of Discipline to Universities of China (No. B06006) and State Key Laboratory of High-efficiency Utilization of Coal and Green Chemical Engineering (2020-KF-26). We also appreciate the stuff in SSRF and BSRF for their help in XAFS data collection and analysis.

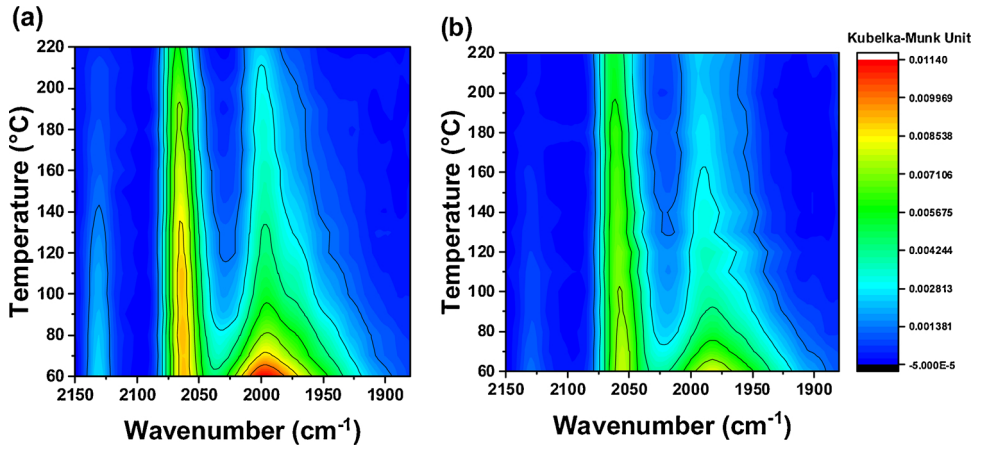

Fig. 13. In situ DRIFTS spectra in the temperature range of 60-220 °C after CO adsorption at 2.0 MPa and 50 °C on the Ru/TiO_2 catalysts: (a) Ru/TiO_2-500-H and (b) Ru/TiO_2-500#-H.

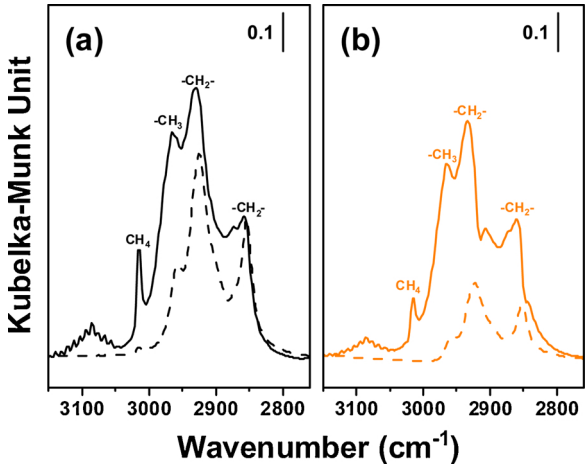

Fig. 14. In situ DRIFTS spectra of (a) Ru/TiO_2-500-H and (b) Ru/TiO_2-500#-H in syngas (H_2/CO = 2) at 2.0 MPa and 220 °C (solid lines) and then purged in He flow for 0.5 h at the same temperature (dash lines).

Appendix A. Supplementary data

Supplementary material related to this article can be found, in the online version, at doi:https://doi.org/10.1016/j.apcatb.2020.119261.

References

[1] W. Zhou, K. Cheng, J. Kang, C. Zhou, V. Subramanian, Q. Zhang, Y. Wang, New horizon in C1 chemistry: breaking the selectivity limitation in transformation of syngas and hydrogenation of CO_2 into hydrocarbon chemicals and fuels, Chem. Soc. Rev. 48 (2019) 3193–3228.
[2] Q. Zhang, K. Cheng, J. Kang, W. Deng, Y. Wang, Fischer–Tropsch catalysts for the production of hydrocarbon fuels with high selectivity, ChemSusChem 7 (2014) 1251–1264.
[3] W. Chen, T. Lin, Y. Dai, Y. An, F. Yu, L. Zhong, S. Li, Y. Sun, Recent advances in the investigation of nanoeffects of Fischer–Tropsch catalysts, Catal. Today 311 (2018) 8–22.
[4] J.L. Eslava, X. Sun, J. Gascon, F. Kapteijn, I. Rodríguez-Ramos, Ruthenium particle size and cesium promotion effects in Fischer–Tropsch synthesis over high-surface-area graphite supported catalysts, Catal. Sci. Technol. 7 (2017) 1235–1244.
[5] J. Kang, S. Zhang, Q. Zhang, Y. Wang, Ruthenium nanoparticles supported on carbon nanotubes as efficient catalysts for selective conversion of synthesis gas to diesel fuel, Angew. Chem. Int. Ed. 48 (2009) 2603–2606.
[6] K. Xiong, J. Li, K. Liew, X. Zhan, Preparation and characterization of stable Ru nanoparticles embedded on the ordered mesoporous carbon material for applications in Fischer–Tropsch synthesis, Appl. Catal. A Gen. 389 (2010) 173–178.
[7] K. Cheng, J. Kang, S. Huang, Z. You, Q. Zhang, J. Ding, W. Hua, Y. Lou, W. Deng, Y. Wang, Mesoporous beta zeolite-supported ruthenium nanoparticles for selective conversion of synthesis gas to C_5–C_{11} isoparaffins, ACS Catal. 2 (2012) 441–449.
[8] A.Y. Khodakov, W. Chu, P. Fongarland, Advances in the development of novel cobalt Fischer–Tropsch catalysts for synthesis of long-chain hydrocarbons and clean fuels, Chem. Rev. 107 (2007) 1692–1744.
[9] J. Yang, W. Ma, D. Chen, A. Holmen, B.H. Davis, Fischer–Tropsch synthesis: a review of the effect of CO conversion on methane selectivity, Appl. Catal. A: Gen. 470 (2014) 250–260.
[10] J. Zhang, H. Wang, L. Wang, S. Ali, C. Wang, L. Wang, X. Meng, B. Li, D.S. Su, F.S. Xiao, Wet-chemistry strong metal–support interactions in titania-supported Au catalysts, J. Am. Chem. Soc. 141 (2019) 2975–2983.
[11] D. Li, N. Ichikuni, S. Shimazu, T. Uematsu, Hydrogenation of CO_2 over sprayed Ru/TiO_2 fine particles and strong metal–support interaction, Appl. Catal. A Gen. 180 (1999) 227–235.
[12] T. Komaya, A.T. Bell, Z. Wengsieh, R. Gronsky, F. Engelke, T.S. King, M. Pruski, Effects of dispersion and metal–metal oxide interactions on Fischer–Tropsch synthesis over Ru/TiO_2 and TiO_2-promoted Ru/SiO_2, J. Catal. 150 (1994) 400–406.
[13] S. Bernal, J.J. Calvino, M.A. Cauqui, G.A. Cifredo, A. Jobacho, J.M. Rodríguez-Izquierdo, Metal–support interaction phenomena in rhodium/ceria and rhodium/titania catalysts: comparative study by high-resolution transmission electron spectroscopy, Appl. Catal. A Gen. 99 (1993) 1–8.
[14] T. Komaya, A.T. Bell, Z. Wengsieh, R. Gronsky, F. Engelke, T.S. King, M. Pruski, The influence of metal–support interactions on the accurate determination of Ru dispersion for Ru/TiO_2, J. Catal. 149 (1994) 142–148.
[15] N. Liu, M. Xu, Y. Yang, S. Zhang, J. Zhang, W. Wang, L. Zheng, S. Hong, M. Wei, $Au\delta^-$–O_v–Ti^{3+} interfacial site: Catalytic active center toward low-temperature water gas shift reaction, ACS Catal. 9 (2019) 2707–2717.
[16] J. Liu, Advanced electron microscopy of metal–support interactions in supported metal catalysts, ChemCatChem 3 (2011) 934–948.
[17] C. Hernandez Mejia, T.W. van Deelen, K.P. de Jong, Activity enhancement of cobalt catalysts by tuning metal–support interactions, Nat. Commun. 9 (2018) 4459–4466.
[18] J.C. Matsubu, S. Zhang, L. DeRita, N.S. Marinkovic, J.G. Chen, G.W. Graham, X. Pan, P. Christopher, Adsorbate-mediated strong metal–support interactions in oxide-supported Rh catalysts, Nat. Chem. 9 (2017) 120–127.
[19] S. Liu, W. Xu, Y. Niu, B. Zhang, L. Zheng, W. Liu, L. Li, J. Wang, Ultrastable Au nanoparticles on titania through an encapsulation strategy under oxidative atmosphere, Nat. Commun. 10 (2019) 5790–5798.
[20] C. Liu, Y. He, L. Wei, Y. Zhang, Y. Zhao, J. Hong, S. Chen, L. Wang, J. Li, Hydrothermal carbon-coated TiO_2 as support for Co-based catalyst in Fischer–Tropsch synthesis, ACS Catal. 8 (2018) 1591–1600.
[21] W. Zhan, Q. He, X. Liu, Y. Guo, Y. Wang, L. Wang, Y. Guo, A.Y. Borisevich, J. Zhang, G. Lu, S. Dai, A sacrificial coating strategy toward enhancement of metal–support interaction for ultrastable Au nanocatalysts, J. Am. Chem. Soc. 138 (2016) 16130–16139.
[22] W. Chen, T.F. Kimpel, Y. Song, F.K. Chiang, B. Zijlstra, R. Pestman, P. Wang, E.J.M. Hensen, Influence of carbon deposits on the cobalt-catalyzed Fischer–Tropsch reaction: evidence of a two-site reaction model, ACS Catal. 8 (2018) 1580–1590.
[23] J.-W. Yu, W.-Z. Li, T. Zhang, D. Ma, Y.-W. Zhang, Ruthenium nanoclusters dispersed on titania nanorods and nanoparticles as high-performance catalysts for aqueous-phase Fischer–Tropsch synthesis, Catal. Sci. Technol. 6 (2016) 8355–8363.
[24] T. Koh, H.M. Koo, T. Yu, B. Lim, J.W. Bae, Roles of ruthenium–support interactions of size-controlled ruthenium nanoparticles for the product distribution of Fischer–Tropsch synthesis, ACS Catal. 4 (2014) 1054–1060.
[25] B. Chen, J.J.G. Goodwin, Isotopic transient kinetic analysis of ethane hydrogenolysis on Cu modified Ru/SiO_2, J. Catal. 158 (1996) 228–235.
[26] B. Ravel, M. Newville, ATHENA, ARTEMIS, HEPHAESTUS: data analysis for X-ray absorption spectroscopy using IFEFFIT, J. Synchrotron Radiat. 12 (2005) 537–541.
[27] Q. Lin, X.Y. Liu, Y. Jiang, Y. Wang, Y. Huang, T. Zhang, Crystal phase effects on the structure and performance of ruthenium nanoparticles for CO_2 hydrogenation, Catal. Sci. Technol. 4 (2014) 2058–2063.
[28] T. Omotoso, S. Boonyasuwat, S.P. Crossley, Understanding the role of TiO_2 crystal

structure on the enhanced activity and stability of Ru/TiO_2 catalysts for the conversion of lignin-derived oxygenates, Green Chem. 16 (2014) 645–652.
[29] J. Wojciechowska, M. Jedrzejczyk, J. Grams, N. Keller, A.M. Ruppert, Enhanced production of gamma-valerolactone with an Internal source of hydrogen on Ca-modified TiO_2 supported Ru catalysts, ChemSusChem 12 (2018) 639–650.
[30] X. Wang, W. Chen, L. Zhang, T. Yao, W. Liu, Y. Lin, H. Ju, J. Dong, L. Zheng, W. Yan, X. Zheng, Z. Li, X. Wang, J. Yang, D. He, Y. Wang, Z. Deng, Y. Wu, Y. Li, Uncoordinated amine groups of metal–organic frameworks to anchor single Ru sites as chemoselective catalysts toward the hydrogenation of quinoline, J. Am. Chem. Soc. 139 (2017) 9419–9422.
[31] J. Xu, X. Su, H. Duan, B. Hou, Q. Lin, X. Liu, X. Pan, G. Pei, H. Geng, Y. Huang, T. Zhang, Influence of pretreatment temperature on catalytic performance of rutile TiO_2-supported ruthenium catalyst in CO_2 methanation, J. Catal. 333 (2016) 227–237.
[32] H. Zhang, J. Cai, Y. Wang, M. Wu, M. Meng, Y. Tian, X. Li, J. Zhang, L. Zheng, Z. Jiang, J. Gong, Insights into the effects of surface/bulk defects on photocatalytic hydrogen evolution over TiO_2 with exposed {001} facets, Appl. Catal. B: Environ. 220 (2018) 126–136.
[33] C.H. Chen, J. Shieh, S.M. Hsieh, C.L. Kuo, H.Y. Liao, Architecture, optical absorption, and photocurrent response of oxygen-deficient mixed-phase titania nanostructures, Acta Mater. 60 (2012) 6429–6439.
[34] J. Choi, H. Park, M.R. Hoffmann, Effects of single metal-ion doping on the visible-light photoreactivity of TiO_2, J. Phys. Chem. C 114 (2010) 783–792.
[35] A. Aitbekova, L. Wu, C.J. Wrasman, A. Boubnov, A.S. Hoffman, E.D. Goodman, S.R. Bare, M. Cargnello, Low-temperature restructuring of CeO_2-supported Ru nanoparticles determines selectivity in CO_2 catalytic reduction, J. Am. Chem. Soc. 140 (2018) 13736–13745.
[36] Y. Guo, S. Mei, K. Yuan, D.-J. Wang, H.-C. Liu, C.-H. Yan, Y.-W. Zhang, Low-temperature CO_2 methanation over CeO_2-supported Ru single atoms, nanoclusters, and nanoparticles competitively tuned by strong metal–support interactions and H-spillover effect, ACS Catal. 8 (2018) 6203–6215.
[37] O.S. Alexeev, S.Y. Chin, M.H. Engelhard, L. Ortiz-Soto, M.D. Amiridis, Effects of reduction temperature and metal − support interactions on the catalytic activity of Pt/γ-Al_2O_3 and Pt/TiO_2 for the oxidation of CO in the presence and absence of H_2, J. Phys. Chem. B 109 (2005) 23430–23443.
[38] T. Nozawa, Y. Mizukoshi, A. Yoshida, S. Naito, Aqueous phase reforming of ethanol and acetic acid over TiO_2 supported Ru catalysts, Appl. Catal. B: Environ. 146 (2014) 221–226.
[39] T.N. Pham, D. Shi, T. Sooknoi, D.E. Resasco, Aqueous-phase ketonization of acetic acid over Ru/TiO_2/carbon catalysts, J. Catal. 295 (2012) 169–178.
[40] W. Grünert, R. Feldhaus, K. Anders, E.S. Shpiro, G.V. Antoshin, K.M. Minachev, Reduction and aromatization activity of chromia-alumina catalysts: II. An XPS investigation of chromia-alumina catalysts, J. Catal. 100 (1986) 138–148.
[41] D.W. Goodman, “Catalytically active Au on Titania”: yet another example of a strong metal support interaction (SMSI)? Catal. Lett. 99 (2005) 1–4.
[42] J. Bao, G. Yang, Y. Yoneyama, N. Tsubaki, Significant advances in C1 catalysis: highly efficient catalysts and catalytic reactions, ACS Catal. 9 (2019) 3026–3053.
[43] X. Yang, W. Wang, L. Wu, X. Li, T. Wang, S. Liao, Effect of confinement of TiO_2 nanotubes over the Ru nanoparticles on Fischer–Tropsch synthesis, Appl. Catal. A Gen. 526 (2016) 45–52.
[44] J.-S. Jung, G.H. Hong, J.I. Park, E.-H. Yang, J.L. Hodala, D.J. Moon, Effect of cobalt supported on meso–macro porous hydrotalcite in Fischer–Tropsch synthesis, RSC Adv. 6 (2016) 104280–104293.
[45] A. Carvalho, M. Marinova, N. Batalha, N.R. Marcilio, A.Y. Khodakov, V.V. Ordomsky, Design of nanocomposites with cobalt encapsulated in the zeolite micropores for selective synthesis of isoparaffins in Fischer–Tropsch reaction, Catal. Sci. Technol. 7 (2017) 5019–5027.
[46] T.W. van Deelen, J.J. Nijhuis, N.A. Krans, J. Zecevic, K.P. de Jong, Preparation of cobalt nanocrystals supported on metal oxides to study particle growth in Fischer–Tropsch catalysts, ACS Catal. 8 (2018) 10581–10589.
[47] T.W. van Deelen, H. Yoshida, R. Oord, J. Zečević, B.M. Weckhuysen, K.P. de Jong, Cobalt nanocrystals on carbon nanotubes in the Fischer-Tropsch synthesis: impact of support oxidation, Appl. Catal. A Gen. 593 (2020) 117441–117448.
[48] M. Casavola, J. Xie, J.D. Meeldijk, N.A. Krans, A. Goryachev, J.P. Hofmann, A.I. Dugulan, K.P. de Jong, Promoted Iron nanocrystals obtained via ligand exchange as active and selective catalysts for synthesis gas conversion, ACS Catal. 7 (2017) 5121–5128.
[49] J.M.G. Carballo, E. Finocchio, S. García-Rodriguez, M. Ojeda, J.L.G. Fierro, G. Busca, S. Rojas, Insights into the deactivation and reactivation of Ru/TiO_2 during Fischer–Tropsch synthesis, Catal. Today 214 (2013) 2–11.
[50] X. Li, J. He, M. Meng, Y. Yoneyama, N. Tsubaki, One-step synthesis of H–β zeolite-enwrapped Co/Al_2O_3 Fischer–Tropsch catalyst with high spatial selectivity, J. Catal. 265 (2009) 26–34.
[51] Q. Cheng, N. Zhao, S. Lyu, Y. Tian, F. Gao, L. Dong, Z. Jiang, J. Zhang, N. Tsubaki, X. Li, Tuning interaction between cobalt catalysts and nitrogen dopants in carbon nanospheres to promote Fischer-Tropsch synthesis, Appl. Catal. B: Environ. 248 (2019) 73–83.
[52] Q. Cheng, Y. Tian, S. Lyu, N. Zhao, K. Ma, T. Ding, Z. Jiang, L. Wang, J. Zhang, L. Zheng, F. Gao, L. Dong, N. Tsubaki, X. Li, Confined small-sized cobalt catalysts stimulate carbon-chain growth reversely by modifying ASF law of Fischer–Tropsch synthesis, Nat. Commun. 9 (2018) 3250–3258.
[53] A.M. Abdel-Mageed, D. Widmann, S.E. Olesen, I. Chorkendorff, J. Biskupek, R.J. Behm, Selective CO methanation on Ru/TiO_2 catalysts: role and influence of metal–support interactions, ACS Catal. 5 (2015) 6753–6763.
[54] M. Zhang, M. Wang, B. Xu, D. Ma, How to measure the reaction performance of heterogeneous catalytic reactions reliably, Joule 3 (2019) 2876–2883.
[55] R. Baetzold, A computational model of the energy of dissociative chemisorption, J. Chem. Phys. 82 (1985) 5724–5731.
[56] C. Elmasides, D.I. Kondarides, S.G. Neophytides, X.E. Verykios, Partial oxidation of methane to synthesis gas over Ru/TiO_2 catalysts: effects of modification of the support on oxidation state and catalytic performance, J. Catal. 198 (2001) 195–207.
[57] P. Panagiotopoulou, D.I. Kondarides, X.E. Verykios, Mechanistic study of the selective methanation of CO over Ru/TiO_2 catalyst: identification of active surface species and reaction pathways, J. Phys. Chem. C 115 (2011) 1220–1230.
[58] C.S. Kellner, A.T. Bell, Infrared studies of carbon monoxide hydrogenation over alumina-supported ruthenium, J. Catal. 71 (1981) 296–307.
[59] F. Solymosi, J. Raskó, An infrared study of the influence of CO adsorption on the topology of supported ruthenium, J. Catal. 115 (1989) 107–119.
[60] S.Y. Chin, C.T. Williams, M.D. Amiridis, FTIR studies of CO adsorption on Al_2O_3- and SiO_2-supported Ru catalysts, J. Phys. Chem. B 110 (2006) 871–882.
[61] C. Elmasides, D.I. Kondarides, W. Grünert, X.E. Verykios, XPS and FTIR study of Ru/Al_2O_3 and Ru/TiO_2 catalysts: reduction characteristics and interaction with a methane − oxygen mixture, J. Phys. Chem. B 103 (1999) 5227–5239.
[62] A.A. Davydov, A.T. Bell, An infrared study of NO and CO adsorption on a silica-supported Ru catalyst, J. Catal. 49 (1977) 332–344.
[63] S.Z. Todorova, G.B. Kadinov, Infrared spectroscopy study of adsorption and coadsorption of carbon monoxide and hydrogen on Ru/Al_2O_3, Res. Chem. Intermed. 28 (2002) 291–301.
[64] W. Wasylenko, H. Frei, Direct observation of the kinetically relevant site of CO hydrogenation on supported Ru catalyst at 700 K by time-resolved FT-IR spectroscopy, Phys. Chem. Chem. Phys. 9 (2007) 5497–5502.
[65] C.S. Kellner, A.T. Bell, Effects of dispersion on the activity and selectivity of alumina-supported ruthenium catalysts for carbon monoxide hydrogenation, J. Catal. 75 (1982) 251–261.
[66] J.T. Yates, T.M. Duncan, S.D. Worley, R.W. Vaughan, Infrared spectra of chemisorbed CO on Rh, J. Chem. Phys. 70 (1979) 1219–1224.
[67] X.-Y. Quek, R. Pestman, R.A. van Santen, E.J.M. Hensen, Structure sensitivity in the ruthenium nanoparticle catalyzed aqueous-phase Fischer–Tropsch reaction, Catal. Sci. Technol. 4 (2014) 3510–3523.
[68] Q. Chang, C. Zhang, C. Liu, Y. Wei, A.V. Cheruvathur, A.I. Dugulan, J.W. Niemantsverdriet, X. Liu, Y. He, M. Qing, L. Zheng, Y. Yun, Y. Yang, Y. Li, Relationship between iron carbide phases (ε-Fe_2C, Fe_7C_3, and χ-Fe_5C_2) and catalytic performances of Fe/SiO_2 Fischer–Tropsch catalysts, ACS Catal. 8 (2018) 3304–3316.
[69] P. Panagiotopoulou, A. Christodoulakis, D.I. Kondarides, S. Boghosian, Particle size effects on the reducibility of titanium dioxide and its relation to the water–gas shift activity of Pt/TiO_2 catalysts, J. Catal. 240 (2006) 114–125.
[70] D. Song, J. Li, Q. Cai, In situ diffuse reflectance FTIR study of CO adsorbed on a cobalt catalyst supported by silica with different pore sizes, J. Phys. Chem. C 111 (2007) 18970–18979.
[71] G. Bian, T. Nanba, N. Koizumi, M. Yamada, Changes in microstructure of a reduced cobalt catalyst during performing FT synthesis from syngas determined by in situ high-pressure syngas adsorption, J. Mol. Catal. A Chem. 178 (2002) 219–228.
[72] M.W. McQuire, C.H. Rochester, FTIR study of CO/H_2 reactions over Ru/TiO_2 and $Ru\text{-}Rh/TiO_2$ catalysts at high temperature and pressure, J. Catal. 157 (1995) 396–402.
[73] Anaëlle Paredes-Nunez, Davide Lorito, Nolven Guilhaume, Claude Mirodatos, Yves Schuurman, F.C. Meunier, Nature and reactivity of the surface species observed over a supported cobalt catalyst under CO/H_2 mixtures, Catal. Today 242 (2015) 178–183.
[74] M. Primet, Electronic transfer and ligand effects in the infrared spectra of adsorbed carbon monoxide, J. Catal. 88 (1984) 273–282.
[75] B.T. Loveless, C. Buda, M. Neurock, E. Iglesia, CO chemisorption and dissociation at high coverages during CO hydrogenation on Ru catalysts, J. Am. Chem. Soc. 135 (2013) 6107–6121.
[76] G.R. Johnson, S. Werner, A.T. Bell, An investigation into the effects of Mn promotion on the activity and selectivity of Co/SiO_2 for Fischer–Tropsch synthesis: evidence for enhanced CO adsorption and dissociation, ACS Catal. 5 (2015) 5888–5903.
[77] P.-Z.M. Josefina, D. Muriel, H. Yann, G. Anne, L. Lucien, L. Ginette, G. Mireya, C.M. Luisa, B. Geoffrey, Characterization and reactivity of Ru/single oxides catalysts for the syngas reaction, Appl. Catal. A Gen. 274 (2004) 295–301.